Can. J. Remote Sensing, Vol. 39, No. 1, pp. 27–33, 2013

Spatio-temporal analysis of ground deformation occurring near Rice Lake, Saskatchewan, and observed by Radarsat-2 DInSAR during 2008–2011

Sergey Samsonov, Pablo J. Gonzalez, Kristy Tiampo, and Nicolas d'Oreye

Abstract. We present ground deformation maps for the southern Saskatchewan region between Rice Lake and the City of Saskatoon measured by Radarsat-2 Differential Interferometric Synthetic Aperture Radar (DInSAR) during 2008–2011. We acquired and processed Radarsat-2 data from two different tracks (Multi-Look Fine beam and one Standard beam) and performed advanced interferometric analysis that revealed ground deformation with a maximum line-of-sight rate close to 10 cm per year. Decomposition of ascending and descending, line-of-sight images into horizontal (mainly east–west) and vertical components revealed the presence of localized horizontal motion with a maximum absolute rate of 4 cm per year and subsidence with a maximum rate of −10 cm per year. These results suggested that simple line-of-sight time series analysis of interferometric data acquired in single geometry is insufficient for capturing a complete pattern of ground deformation and can be misleading in the presence of both horizontal and vertical components of deformation.

Résumé. On présente des cartes de déformations du sol pour la région du sud de la Saskatchewan, entre Rice Lake et la ville de Saskatoon, mesurées à l'aide des données d'interférométrie différentielle radar à synthèse d'ouverture (DInSAR) de RADARSAT-2, entre 2008 et 2011. On a fait l'acquisition et traité des données de RADARSAT-2 en utilisant deux modes différents (faisceau fin à multivisée et un faisceau standard) et on a réalisé une analyse interférométrique avancée qui a permis de révéler des déformations du sol avec un taux maximum en visée directe de près de 10 cm/an. La décomposition des images ascendantes et descendantes en visée directe en composantes horizontales (surtout est-ouest) et verticales a révélé la présence de mouvement horizontal localisé avec un taux maximum absolu de 4 cm/an et une subsidence avec un taux maximum de −10 cm/an. Ces résultats indiquent qu'une simple analyse des séries chronologiques d'images en visée directe des données interférométriques acquises en géométrie unique est insuffisante pour donner un patron complet des déformations du sol et que cela peut engendrer une certaine confusion en présence de composantes horizontales et verticales des déformations.
[Traduit par la Rédaction]

Introduction

Differential Synthetic Aperture Radar Interferometry (DInSAR) is an established methodology for mapping ground deformation (Massonnet and Feigl, 1998; Rosen et al., 2000). An interferogram is a conjugate product of two coregistered complex SAR images acquired by the same or a similar sensor at two different times. After removing Earth's curvature and topographic components, the remaining signal in a DInSAR image (also called a differential interferogram) is proportional to the ground deformation that occurred between image acquisitions (Massonnet and Feigl, 1998; Rosen et al., 2000; Samsonov et al., 2010, 2011a). Interferograms are usually contaminated by the atmospheric noise related to travel time delays caused by fluctuations of water vapor in the troposphere and electron content in the ionosphere (Hanssen and Feijt, 1996; Li et al., 2005). In a single differential interferogram, deformation and atmospheric signals are indistinguishable.

The Small Baseline Subset (SBAS) methodology (Berardino et al., 2002; Usai, 2003; Lanari et al., 2004; Samsonov et al., 2011b) was developed to reduce undesirable signals (atmospheric, orbital, and thermal noise) by computing a

Received 7 May 2012. Accepted 15 February 2013. Published on the Web at http://pubs.casi.ca/journal/cjrs on 15 May 2013.

Sergey Samsonov.[1] Canada Centre for Remote Sensing, 588 Booth Street, Ottawa, ON K1A 0Y7, Canada.

Pablo J. Gonzalez and Kristy Tiampo. Department of Earth Sciences, University of Western Ontario, London, ON N6A 5B7, Canada.

Nicolas d'Oreye. European Center for Geodynamics and Seismology, Rue Josy Welter 19, L-7256 Walferdange, Grand-Duchy of Luxembourg and National Museum of Natural History, Dept. Geophysics/Astrophysics, Rue Josy Welter 19, L-7256 Walferdange, Grand-Duchy of Luxembourg.

[1]Corresponding author (e-mail: sergey.samsonov@nrcan-rncan.gc.ca).

least squares solution from many interferograms acquired under favorable conditions (e.g., small temporal and spatial baselines). The solution produced by SBAS is time series of line-of-sight (LOS) displacements for each pixel in a SAR image and linear deformation rate maps calculated by applying a linear regression to calculated time series.

For a single acquisition geometry, in the absence of additional information, the SBAS LOS solution cannot be decomposed into the three components of ground displacement vector (e.g. north, east, up) that would comprise a complete solution. However, if SAR data from more than one acquisition geometry are available, then the SBAS methodology can be modified to produce an approximate solution consisting of time series and linear deformation rates of more than one component (Samsonov and d'Oreye, 2012).

In this study, we analyzed the surface ground deformation in a southern Saskatchewan region between Rice Lake and the City of Saskatoon. This region is characterized by approximately an 80–100 m succession of tertiary to quaternary age sediments of glacial origin (till, clay, silt, sand, and gravel) developed over a cretaceous age basement rocks. The terrain surface area is mainly covered by agricultural fields, with extensive water bodies due to the shallow groundwater table level. Here we produced time series and corresponding linear deformation rate maps calculated with standard SBAS and multidimensional SBAS (MSBAS) techniques (Samsonov and d'Oreye, 2012) and observed regions of ground deformation consisting of both vertical and horizontal motion. Modeling of these deformations will be addressed in ongoing work; here we concentrated mainly on introducing a processing methodology that can be used as a guideline for similar studies in Canada and elsewhere. We do not identify the causes of these signals.

Methodology

In this study we demonstrated the application of the SBAS proposed by Berardino et al. (2002) and Usai (2003) and the MSBAS proposed by Samsonov and d'Oreye (2012).

In the case of a single set of SAR images acquired by a sensor with an azimuth α and an incidence angle θ, the time series of deformation can be reconstructed by applying the following methodology:

$$A V_{\text{los}} = \Phi_{\text{obs}}, \quad V_{\text{los}} = A^{+}\Phi_{\text{obs}}, \quad d_{\text{los}}^{i+1} = d_{\text{los}}^{i} + v_{\text{los}}^{i+1}\Delta t^{i+1} \tag{1}$$

where A is a matrix constructed from the time intervals between consecutive SAR acquisitions (Samsonov, 2010; Samsonov et al., 2011b), V_{los} is a vector of the unknown line-of-sight velocities, Φ_{obs} is a vector of observed interferogram values, A^{+} is a pseudo-inverse of matrix A found by applying the Singular Value Decomposition (SVD), and d_{los}^{i} is a line-of-sight displacement at the time t^{i}.

For the case of K multiple SAR sets acquired by sensors with different orbital parameters (e.g., azimuth and incidence angles), Equation (1) can be rewritten in the following form for each set with $k = 1 \ldots K$

$$\left|S_N^k A \quad S_E^k A \quad S_U^k A\right| \times \left|V_N \quad V_E \quad V_U\right|^{\mathrm{T}} = \Phi_{\text{obs}}^k \tag{2}$$

assuming that $V_{\text{los}} = \mathbf{SV} = S_N V_N + S_E V_E + S_U V_U$ and $\mathbf{S} = \{S_N, S_E, S_U\} = \{\sin\alpha \sin\theta, -\cos\alpha \sin\theta, \cos\theta\}$, where $\mathbf{S}$ is a line-of-sight unit vector with north, east, and up components S_N, S_E, S_U, respectively, and $\mathbf{V}$ is a velocity (ground deformation rate) vector with components V_N, V_E, V_U.

The MSBAS method that includes all K sets of independently acquired SAR data can be presented in the following form

$$\begin{pmatrix} A^1 \\ A^2 \\ \ldots \\ A^K \end{pmatrix} \begin{pmatrix} V_N \\ V_E \\ V_U \end{pmatrix} = \begin{pmatrix} \Phi^1 \\ \Phi^2 \\ \ldots \\ \Phi^K \end{pmatrix} \text{ or } \hat{\mathbf{A}}\hat{\mathbf{V}}_{\text{los}} = \hat{\Phi}_{\text{obs}} \tag{3}$$

where the new matrix $\hat{\mathrm{A}}$ (as in Equation (2)) has dimensions $3\left(\sum_{k=1}^{K} N^k - 1\right) \times \sum_{k=1}^{K} M^k$, the new vector V has dimensions $1 \times 3\left(\sum_{k=1}^{K} N^k - 1\right)$, and the new vector Φ_{obs} has dimensions $1 \times \sum_{k=1}^{K} M^k$. Here N^k corresponds to the number of single-look complex (SLC) images and M^k corresponds to the number of interferograms from dataset k.

This problem usually is underdetermined because the number of linearly independent equations is less than the number of unknown velocities. Indeed, if all SAR images were acquired at different times t^{i}, then the number of unknowns would be equal to $3\left(\sum_{k=1}^{K} N^k - 1\right)$ and the maximum possible number of independently observed interferograms would be equal to $\left(\sum_{k=1}^{K} N^k - K\right)$. All modern space-borne SAR systems orbit the Earth in a near-polar orbit and can acquire data only in two independent acquisition geometries: ascending and descending. Such acquisition geometries are insensitive to a motion in the northerly direction (i.e., along track). Therefore, the number of unknowns in Equation (3) is reduced to $2\left(\sum_{k=1}^{K} N^k - 1\right)$ by excluding all terms responsible for northern motion V_N. This approximation is reasonable when the magnitude of the north–south component of deformation is comparable to (not significantly larger than) the magnitude of the east–west and vertical components. In Samsonov and d'Oreye (2012) we estimated the precision of this technique when north–south motion is present and of the same magnitude as east–west motion. We showed that reduction in precision is minimal and certainly below the level that can affect the interpretation of results on a qualitative level.

The solution of the problem stated by Equation (3) can be further regularized by applying Tikhonov regularization (Tikhonov and Arsenin, 1977) in the following form:

$$\begin{pmatrix} \hat{A} \\ \lambda I \end{pmatrix} \begin{pmatrix} V_E \\ V_U \end{pmatrix} = \begin{pmatrix} \hat{\Phi} \\ 0 \end{pmatrix} \quad (4)$$

where λ is a regularization parameter that can be found, for example, using the L-curve method (Hansen and O'Leary, 1993) and I is a $2\left(\sum_{k=1}^{K} N^k - 1\right) \times 2\left(\sum_{k=1}^{K} N^k - 1\right)$ identity matrix.

Data and results

For this study we collected the following Radarsat-2 data: 23 Multi-Look Fine 3F (MF3F) beam spanning from 27 October 2008 to 23 December 2011 and 15 images from Standard 3 (S3) beam spanning from 29 September 2008 to 21 August 2011. Images from each beam were processed independently in the following way. One image for each beam was selected as master and the remaining images were coregistered to the selected master. All possible interferograms with perpendicular baselines less than 400 m were created. The topographic phase was removed using 20 m digital elevation model (DEM) from GEOBASE CDEM database (http://www.geobase.ca) with an approximate reported elevation accuracy of 5 m. Differential interferograms were filtered and unwrapped. Additional processing steps such as orbital correction (e.g., removal of linear or quadratic trend) and phase interpolation over incoherent regions also were performed to increase the quality and the coverage of the interferograms. Finally, corrected interferograms were geocoded to the DEM grid. It was noticed that accuracy of the geocoding was low for some master images and several attempts were required to find master images with accurate state vectors.

We analyzed the mean coherence for each interferogram and selected only those interferograms that had a mean coherence (after filtering) above 0.5 for further processing. Selected interferograms were checked for unwrapping errors and a few low quality interferograms were removed. For time series analysis we selected 29 and 23 interferograms from corresponding MF3F and S3 beams, respectively, as shown in **Table 1**.

First, the standard SBAS methodology (Equation (1)) (Samsonov et al., 2011b) was applied. Here we solved only for deformation rates assuming that the residual topographic component was sufficiently small because of the high accuracy of the available DEM and the small perpendicular baseline of selected interferograms. Time series were recreated by integration from calculated velocities and the linear deformation rate was reconstructed by applying a linear regression to the calculated time series. No temporal or spatial filtering was applied.

Table 1. SAR datasets used in this work.

InSAR set	Time span	α°	θ°	N	M
MF3F, (ascending)	27 October 2008 – 23 December 2011	−9	45	23	29
S3, (descending)	29 September 2008 – 21 August 2011	−169	36	15	23

Note: α, azimuth angle; θ, incidence angle, N, number of available SAR images; and M, number of used interferograms.

Further processing was limited to a subregion outlined in red in **Figure 1**. The small region of subsidence with a maximum rate close to −4 cm per year, located at 51.912N, 107.051W (most southern in **Figure 1**), observed by the MF3F beam is not discussed here because of limited coverage by the single beam.

The deformation map from the MF3F beam shows two regions of motion in the direction away from the satellite (i.e., apparent subsidence). The largest subsidence consists of two nearly circular regions of motion with maximum rates close to −10 cm per year located at 52.078N, 107.067W (left) and 52.083N, 107.032W (right). The centers of these regions are marked as points A1 and A2 in **Figure 2a**. The second region of apparent subsidence, point A4, is located east of the largest subsidence at 52.118N, 106.845W, with a rate close to −4 cm per year. The deformation time series for these regions are shown in **Figure 2c**. Point A3, located in an apparently stable region on the eastern flank of the largest subsidence, does not display any significant motion. The temporal variability in the time series is insignificant and probably is due to atmospheric, orbital, and unwrapping errors partially caused by seasonal changes (snow coverage and moisture redistribution).

The deformation map produced from the S3 beam is shown in **Figure 2b**. As in the previous case, central subsidence consists of two nearly circular regions of motion. Here the centers are marked as points B1 and B2 that are collocated precisely with points A1 and A2 from **Figure 2a**. The second subsidence, point B4, located east of the largest subsidence (collocated precisely with A4), exhibits motion with a rate close to −4 cm per year. Point B3 (collocated precisely with A3), here shows apparent subsidence with a rate close to −4 cm per year. The time series of deformation for points B1–B4 are shown in **Figure 2d**. It is reasonable to assume that minor temporal variability in these time series is caused by atmospheric, orbital, and unwrapping errors, and the rate of motion during the observation period can be considered constant with a high degree of confidence.

To estimate precision of linear deformation rates shown in **Figures 2a** and **2b** we masked out regions with a magnitude of ground deformation greater than 2 cm per year and calculated the standard deviation for the remaining area assuming that ground is stable. Deformation signal with a magnitude larger than 2 cm per year was considered to be the true deformation signal located only in areas described previously. In this way we estimated standard deviation of 0.33 cm per year and 0.43 cm per year for MF3F and S3 beams correspondingly and the root mean square error between both beams of 0.42 cm per year. Clearly the

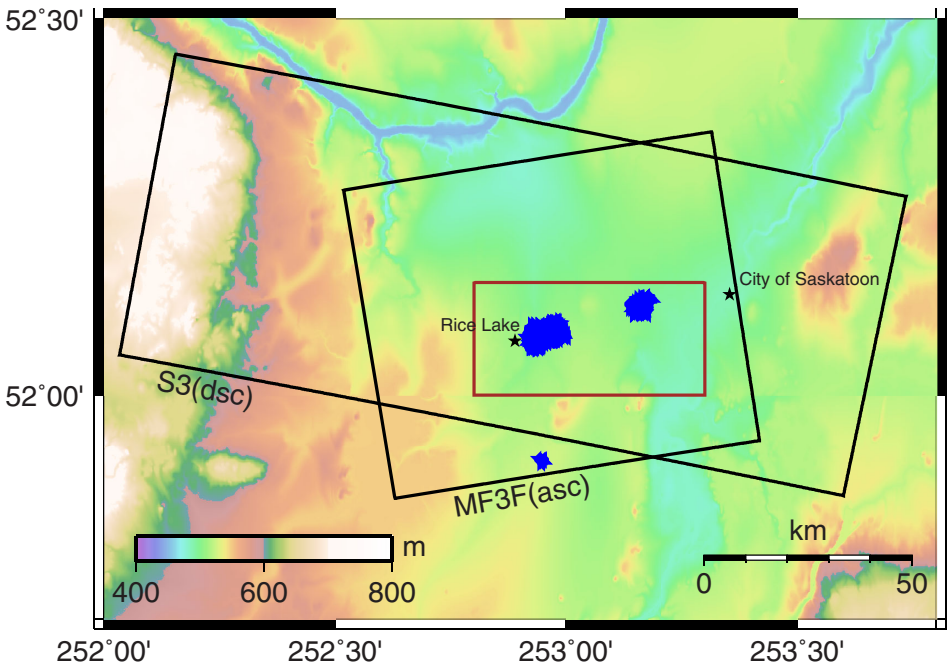

Figure 1. Area of interest, southern Saskatchewan. Background is 20 m Digital Elevation Model. Footprint of Radarsat-2 images used in this study is outlined in black. Regions of fast subsidence (greater than −2.0 cm per year as observed by MF beams and greater than −2.5 cm per year as observed by S3 beam) marked in blue. Most southern subsidence was not studied in this paper because of limited coverage by only one MF3F beam.

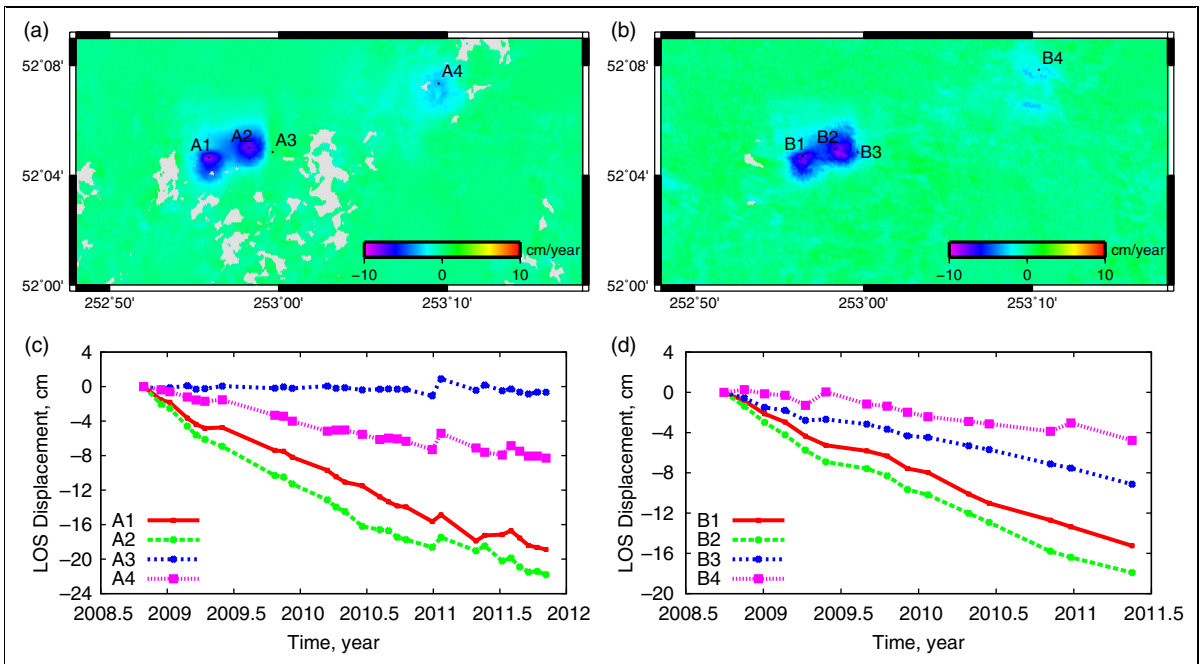

Figure 2. Line-of-sight (LOS) linear deformation rate calculated from Radarsat-2 (a) MF3F SAR images acquired between 27 October 2008 and 29 November 2011 and (b) S3 SAR images acquired between 29 September 2008 and 21 August 2011 with corresponding time series plotted for 15 × 15 pixels regions marked by points A1–A4 and B1–B4 (c–d). Light gray patches are incoherent regions for which measurement of ground deformation was impossible. Superior coverage was achieved by minor interpolation of unwrapped phase in individual interferograms prior to applying SBAS processing.

observed deformation signal was significantly above the subcentimetre noise level.

Comparison of time series for points A3 and B3, which are located at precisely the same location, suggests that the observed deformation signal is not entirely vertical. Indeed, from **Figure 2d**, it is clear that point B3 experiences significant motion away from the satellite, which is situated to the south-east (descending right-looking geometry). On the other hand, **Figure 2c** does not show any significant motion, while the satellite is situated to the south-west of the region in this case (ascending, right-looking geometry). Such a deformation pattern can be explained by the presence of both vertical downward and horizontal westward motion, as was discussed in detail in Samsonov et al. (2011a).

To validate this hypothesis and to measure horizontal and vertical deformation rates with the corresponding time series, we performed multidimensional time series analysis using the MSBAS technique (Equation (4)) (Samsonov and d'Oreye, 2012) applied to ascending MF3F and descending S3 beams simultaneously. These results are shown in **Figure 3**. Time series of ground deformation now clearly display horizontal eastward motion for points 1, 2, and 4 and westward motion for point 3.

It is worth mentioning that precise referencing of all datasets is required for the MSBAS processing. This can be performed either during the standard InSAR processing by selecting the same DEM grid, or during the post-processing using, for example, the generic mapping tools (GMT) scripts (Wessel and Smith, 1998) for resampling to the common grid. For our purposes, we believe that both approaches produce similar results; however, the first method is more efficient and less time consuming.

We further compared linear deformation maps calculated using the MSBAS technique with linear deformation maps

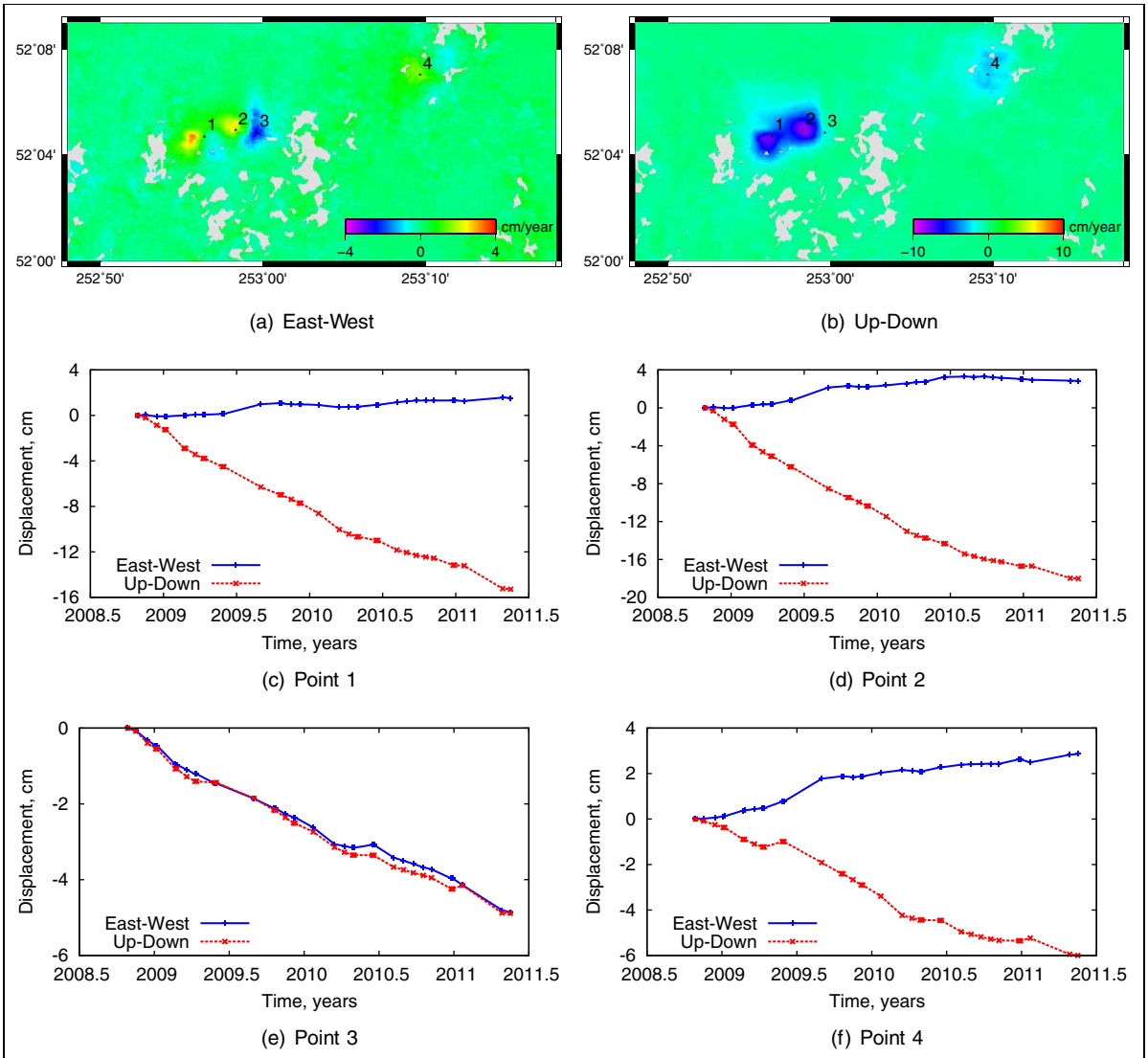

Figure 3. Horizontal east–west (a) and vertical up–down (b) linear deformation rate calculated using MSBAS technique with corresponding time series plotted for 15 × 15 pixels regions marked by points 1–4 (c–d). Light gray patches in (a) and (b) are incoherent regions for which measurement of ground deformation was impossible.

calculated from a combination of ascending and descending data processed independently assuming the methodology of Manzo et al. (2006). We observed root mean square errors for east–west and vertical components corresponding to 0.27 cm and 0.25 cm.

Conclusions

In this paper we demonstrated the application of SBAS and MSBAS techniques for mapping ground deformation in the southern Saskatchewan region between Rice Lake and the City of Saskatoon measured by Radarsat-2 DInSAR during 2008–2011.

We presented a methodology for combining ascending and descending InSAR data to calculate two-dimensional time series of ground deformation. However, the technique can be used for the integration of an unlimited number of InSAR datasets from sensors with different acquisition parameters including azimuth and incidence angles, temporal and spatial sampling and resolution, wave-length, and various polarizations, both air-borne and space-borne.

The proposed method has four main advantages: (*i*) it achieves combined temporal coverage over an extended period of time when data from various beams and (or) sensors with different temporal coverage is available; (*ii*) temporal resolution of the resulting time series increases because it includes the combined sampling from all datasets, which helps to observe the signal in greater detail and also improves the quality of post-processing (i.e., filtering); (*iii*) two or three (depending on acquisition geometry and number of available datasets) components of the ground deformation vector are computed, which helps in the interpretation of observed ground deformation and further modeling and inversion; and (*iv*) various sources of noise (i.e., tropospheric, ionospheric, topographic, orbital, thermal, etc.) are averaged out during the processing improving the signal-to-noise ratio.

In addition to the advantages outlined, simultaneous analysis of ascending and descending DInSAR results allows for cross-validation of each individual dataset. This can be very valuable for studying remote regions that do not have any ground measurements that can be used for independent validation of DInSAR results. Initial attempts to identify the causes of this deformation suggest they are anthropogenic in nature and probably related to groundwater extraction. Further work will be directed towards modeling these signals for derivation of geophysical parameters such as volume of extracted fluids, precise location, and depth.

Acknowledgements

We acknowledge a contribution of the Canadian Space Agency that provided Radarsat-2 data. We would like to thank C. Rogal from Saskatchewan Watershed Authority; R. Horzog, W. Kotyk, B. Sigurdson, and R. Troyer from Government of Saskatchewan; J. Sundquist from Agrium; M. Getzlaf from Potash Corp.; and J. Adams from TransGas for providing valuable information about mining and groundwater related activities in this region. KFT and PJG are supported by an NSERC Discovery Grant. Images presented in this paper were prepared using the Generic Mapping Tool developed by Paul Wessel and Walter H. F. Smith. We also would like to thank N. Short and V. Singhroy for their valuable suggestions for improving this manuscript. ESS contribution number is 20120075.

References

Berardino, P., Fornaro, G., and Lanari, R. 2002. A new algorithm for surface deformation monitoring based on small baseline differential SAR interferograms. *IEEE Transactions on Geoscience and Remote Sensing*, Vol. 40, No. 11, pp. 2375–2383. doi: 10.1109/TGRS.2002.803792.

Hansen, P., and O'Leary, D. 1993. The use of the L-curve in the regularization of descrete ill-posed problems. *SIAM Journal on Scientific Computing*, Vol. 14, No. 6, pp. 1487–1503. doi: 10.1137/0914086.

Hanssen, R., and Feijt, A. 1996. A first quantative evaluation of atmospheric effects on SAR interferometry. In *Proceedings of the Fringe 96 Workshop, Zurich, Switzerland*.

Lanari, R., Mora, O., Manunta, M., Mallorqui, J.J., Berardino, P., and Sansosti, E. 2004. A small-baseline approach for investigating deformations on full-resolution differential SAR interferograms. *IEEE Transactions on Geoscience and Remote Sensing*, Vol. 42, No. 7, pp. 1377–1386. doi: 10.1109/TGRS.2004.828196.

Li, Z., Muller, J.-P., Cross, P., and Fielding, E.J. 2005. Interferometric synthetic aperture radar (InSAR) atmospheric correction: GPS, Moderate Resolution Imaging Spectroradiometer (MODIS), and InSAR integration. *Journal of Geophysical Research*, Vol. 110, No. B03410. doi: 10.1029/2004JB003446.

Manzo, M., Ricciardi, G., Casu, G.F., Zeni, G., Borgstrom, S., Berardino, P., Del Gaudio, C., and Lanari, R. 2006. Surface deformation analysis in the Ischia Island (Italy) based on spaceborne radar interferometry. *Journal of Volcanology and Geothermal Research*, Vol. 151, pp. 399–416. doi: 10.1016/j.jvolgeores.2005.09.010.

Massonnet, D., and Feigl, K. 1998. Radar interferometry and its application to changes in the Earth surface. *Reviews of Geophysics*, Vol. 36, No. 4, pp. 441–500. doi: 10.1029/97RG03139.

Rosen, P., Hensley, P., Joughin, I., Li, F., Madsen, S., Rodriguez, E., and Goldstein, R. 2000. Synthetic aperture radar interferometry. *Proceedings of the IEEE*, Vol. 88, No. 3, pp. 333–382. doi: 10.1109/5.838084.

Samsonov, S. 2010. Topographic correction for ALOS PALSAR interferometry. *IEEE Transactions on Geoscience and Remote Sensing*, Vol. 48, No. 7, pp. 3020–3027. doi: 10.1109/TGRS.2010.2043739.

Samsonov, S., and d'Oreye, N. 2012. Multidimensional time series analysis of ground deformation from multiple InSAR data sets applied to Virunga Volcanic Province. *Geophysical Journal International*, Vol. 191, No. 3, pp. 1095–1108. doi: 10.1111/j.1365-246X.2012.05669.x.

Samsonov, S., Tiampo, K., Gonzalez, P., Manville, V., and Jolly, G. 2010. Modelling deformation occurring in the city of Auckland, New Zealand mapped by the Differential Synthetic Aperture Radar. *Journal of*

Geophysical Research – Solid Earth, Vol. 115, No. B08410. doi: 10.1029/2009JB006806.

Samsonov, S., Beavan, J., Gonzalez, P., Tiampo, K., and Fernandez, J. 2011a. Ground deformation in the Taupo Volcanic Zone, New Zealand observed by ALOS PALSAR interferometry. *Geophysical Journal International*, Vol. 187, No. 1, pp. 147–160. doi: 10.1111/j.1365-246X.2011.05129.x.

Samsonov, S., van der Koij, M., and Tiampo, K. 2011b. A simultaneous inversion for deformation rates and topographic errors of DInSAR data utilizing linear least square inversion technique. *Computers and Geosciences*, Vol. 37, No. 8, pp. 1083–1091. doi: 10.1016/j.cageo.2011.01.007.

Tikhonov, A.N., and Arsenin, V.Y. 1977. *Solution of Ill-posed problems.* John Wiley & Sons.

Usai, S. 2003. A least squares database approach for sar interferometric data. *IEEE Transactions on Geoscience and Remote Sensing*, Vol. 41, No. 4, pp. 753–760. doi: 10.1109/TGRS.2003.810675.

Wessel, P., and Smith, W. 1998. New, improved version of the generic mapping tools released. *EOS Transactions, AGU*, Vol. 79, 579 pp.